

Effects of TaN, Ru, and Pt electrodes on thermal stability of hafnium-based gate stacks

Jinhee Kwon and Yves J. Chabal

Citation: [Journal of Applied Physics](#) **107**, 123505 (2010); doi: 10.1063/1.3429238

View online: <http://dx.doi.org/10.1063/1.3429238>

View Table of Contents: <http://scitation.aip.org/content/aip/journal/jap/107/12?ver=pdfcov>

Published by the [AIP Publishing](#)

Articles you may be interested in

[Oxygen migration induced resistive switching effect and its thermal stability in W/TaO_x/Pt structure](#)
Appl. Phys. Lett. **100**, 253509 (2012); 10.1063/1.4730601

[Thermal stability of lanthanum in hafnium-based gate stacks](#)
J. Appl. Phys. **106**, 053506 (2009); 10.1063/1.3190505

[Study on characteristics of thermally stable HfLaON gate dielectric with TaN metal gate](#)
Appl. Phys. Lett. **93**, 252903 (2008); 10.1063/1.3050522

[Effect of nitrogen content in Hf_xTa_yN metal gate on work function and thermal stability of advanced metal-oxide-semiconductor devices](#)
Appl. Phys. Lett. **90**, 132101 (2007); 10.1063/1.2716311

[Improved barrier properties of ultrathin Ru film with TaN interlayer for copper metallization](#)
Appl. Phys. Lett. **88**, 151912 (2006); 10.1063/1.2195112

 **SHIMADZU**
Excellence in Science

Powerful, Multi-functional UV-Vis-NIR and FTIR Spectrophotometers

Providing the utmost in sensitivity, accuracy and resolution for applications in materials characterization and nano research

- Photovoltaics
- Polymers
- Thin films
- Paints
- Ceramics
- DNA film structures
- Coatings
- Packaging materials

[Click here to learn more](#)

Four Shimadzu spectrophotometers are shown. From left to right: a small benchtop model, a larger benchtop model with a sample holder, a large floor-standing model with a double door, and another large floor-standing model with a single door.

Effects of TaN, Ru, and Pt electrodes on thermal stability of hafnium-based gate stacks

Jinhee Kwon^{a)} and Yves J. Chabal

Department of Materials Science and Engineering, University of Texas at Dallas, 800 W. Campbell Road, RL 10, Richardson, Texas 75080, USA

(Received 18 December 2009; accepted 20 April 2010; published online 16 June 2010)

Potential p-FET high-work function metals, TaN, Ru, and Pt are shown to have distinct effects on the stability of Hf-based gate stacks during a thermal process. Ru and Pt promote catalytic decomposition of the underlying dielectrics, resulting in the formation of HfSi_x and Ru(Pt)Si_x at 950 (900) °C. With Ru, hydroxyl impurities are critical in silicidation which is localized in the vicinity of voids where the Si substrate is exposed through partial HfO_2 and SiO_2 decomposition. The degree of silicide formation is greater with Pt, occurring upon major decomposition of the underlying dielectrics with or without hydroxyl impurities. Transfer of electrons from the HfO_2 oxygen vacancy to Ru and Pt may play a role in the decomposition of the dielectric films. In contrast, the thermal evolution of TaN-gate stacks is very similar to that of HfO_2 stacks without any capping metal layer. With annealed HfO_2 and HfO_2/TaN stacks there is no detectable metal diffusion into the dielectrics, and the overall compositional stability is preserved except for the growth of interfacial SiO_2 . © 2010 American Institute of Physics. [doi:10.1063/1.3429238]

I. INTRODUCTION

Metal gate electrodes with high-permittivity (κ) dielectrics are required for scaling of complementary metal oxide semiconductor (CMOS) devices. Tantalum nitride (TaN), ruthenium (Ru), and platinum (Pt) are potential transition metals for gate electrodes in p-channel field-effect transistors (p-FETs) due to their high work function and theoretical chemical/thermodynamic stability in contact with high- κ HfO_2 gate dielectrics. In particular, composition and interface stability under typical CMOS thermal cycling conditions is a key concern for electrical device performances. But contrary to the expected interfacial stability predicted by thermodynamics, there have been extensive reports about film decomposition and interdiffusion of elements upon annealing. HfO_2 decomposes and reacts with Si to form hafnium silicide despite the presence of interfacial SiO_2 at the temperature as low as 750 °C.^{1,2} However, depending on the nature of the environment, annealing HfO_2 can also end up with additional interfacial layer growth due to diffusion of excess oxygen.³ Gaumer *et al.*⁴ reported oxygen and nitrogen diffusion between HfO_2 and TaN layers under spike annealing, and Sugimoto *et al.*⁵ observed Ta oxide formation at the HfO_2/TaN interface. A thermal process can result in massive interdiffusion at both interfaces of Ru/Hf-based dielectric gate stacks⁶ but may have negligible effects with Pt.⁷ On the contrary Copel *et al.*⁸ observed reduction in HfO_2 with the Pt overlayer using x-ray photoelectron spectroscopy (XPS).

Information found in the literature regarding thermal stability of gate stacks is varied because the thermal evolution depends on many parameters such as film thickness, oxygen concentration in and around the gate stack, annealing temperature, duration, and treatment history before annealing. Moreover, interactions occurring both in the bulk and at the

metal/high- κ and high- κ/SiO_2 and Si interfaces upon annealing are strongly dependent on the nature of metal overlayers. In order to develop a comparative overview of the chemical nature and thermal stability of p-FET metals in contact with HfO_2 , it is important to carry out sample preparation and annealing under identical conditions.

In this work we study the thermal evolution of HfO_2 -based gate stacks with three potential p-FET metal electrodes, TaN, Ru, and Pt upon annealing up to 950 °C in nitrogen. Using *in situ* infrared vibrational spectroscopy, we explore metal diffusion, dielectric quality, and interface evolution for the full CMOS stack during anneal. Direct information of chemical bonding evolution of dielectric layers (HfO_2 , SiO_2) is provided by infrared absorption spectra that are sensitive to crystallization, decomposition of metal-oxygen bonds, and interfacial layer formation and phase changes. Compositional and morphological changes after annealing are investigated by using *ex situ* surface characterization techniques such as x-ray diffraction (XRD), x-ray photoemission spectroscopy (XPS), and atomic force microscopy (AFM). Mechanisms for interface/bulk degradation upon annealing with different metal gates are derived from these complementary data.

II. EXPERIMENTAL

Double side polished Czochralski grown silicon wafers ($\sim 10 \text{ } \Omega \cdot \text{cm}$) were used as the substrate. Thin HfO_2 (4 nm thick) layers were grown on thin thermal oxide (2–3 nm thick SiO_2) by atomic layer deposition. Three different metal layers, TaN, Ru, and Pt were deposited (2 nm) by physical vapor deposition (PVD) in an external system. One of the HfO_2 samples was not capped with any metal to be used as a reference. Thermal annealing was carried out in ultrapure N_2 ambient (oxygen impurity $< 10^{-3}$ ppm) at 8 Torr up to 950 °C for 20 s. The evolution of thermal effects on the

^{a)}Electronic mail: jinhee@utdallas.edu.

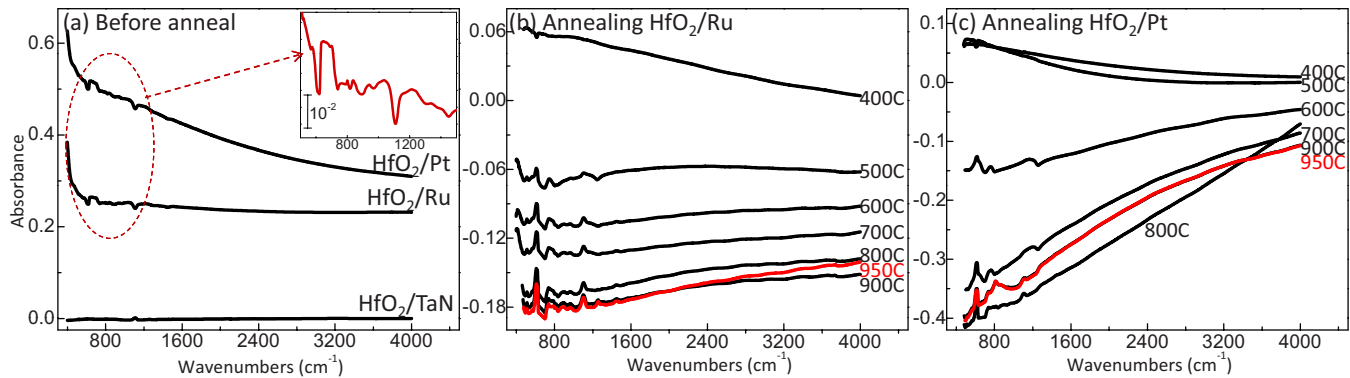


FIG. 1. (Color online) (a) Infrared absorbance spectra of as-deposited HfO_2/Ta , HfO_2/Ru , and HfO_2/Pt referenced to that of the HfO_2 film without metal layers before any thermal process. [(b) and (c)] show absorbance spectra of HfO_2/Ru and HfO_2/Pt , respectively, annealed up to 950°C with 100°C (or 50°C) increment referenced to each initial surface spectrum before annealing. They are in common scale without baseline correction or vertical shift. The inset in (a) is the expanded silicon phonon modes from the circled range.

stacks was studied by *in situ* Fourier transform infrared spectroscopy (FTIR) measured by a Thermo Nicolet 670 interferometer. Single-pass transmission geometry was used with an incidence angle close to the Brewster angle and normal incidence to help distinguish polarization of infrared vibrational modes in absorbance spectra. The substrate temperature during infrared absorbance measurements was maintained at 60°C with a temperature control within 0.5°C to suppress any thermal artifacts from bulk Si phonon vibrations. The oxidation state of each element was studied by *ex situ* XPS using an Al $K\alpha$ source (Perkin-Elmer 5300). A Rigaku Ultima III XRD system was used for grazing incidence XRD for crystallinity study. The surface morphology before and after annealing was imaged by a Veeco Nanoscope 3D AFM.

III. RESULTS AND DISCUSSION

A. Infrared absorbance spectroscopy

Broadband IR absorbance spectra are particularly useful to investigate the conductivity variations in metal films (Sec. III A 1) and the evolution of the chemical bonding of dielectric layers (Sec. III A 2) upon annealing. When thin metal films on semiconductors are studied, an optical effect needs to be taken into account because it greatly affects the spectra. Since this effect has not been widely recognized so far, a Sec. III A 3 is dedicated to its origin and explanation.

1. Conductivity changes in metal gates

The most frequently used IR spectroscopic methods to study absorbates on metallic substrates are grazing incidence reflection (especially for thick metal films) or attenuated total reflection using an external Ge prism. However, due to the need to probe the metallic film itself and metal/high- κ and high- κ/SiO_2 and SiO_2/Si interfaces together with the bulk of dielectrics and silicon, transmission IR spectroscopy is used as the optimum methodology for *in situ* tracking of thermal gate stack evolution. Even though light transmission diminishes quickly in metallic films due to their large extinction coefficients, the transmission level through ultrathin metallic films is sufficient enough in the infrared region to perform spectroscopic studies. A metal thickness of 2 nm is much smaller than the skin depth ($\sim 20\text{--}30$ nm) in the given fre-

quency range, so that $\sim 50\%$ (40% at lower energies) of infrared beam is transmitted through HfO_2/Ru and $\sim 40\%$ (20% at lower energies) through HfO_2/Pt relative to the HfO_2 film (100%) as shown in the absorbance spectra in Fig. 1(a).

Figure 1 shows primarily the broadband variation in the absorption spectra. The broadband absorption is either due to scattering losses arising from inhomogeneities or to the excitation of electronic transitions within the deposited film. Scattering is most significant when small aggregates of material characterized by a high index of refraction (e.g., metallic particles) are formed. Scattering results in dominance of high frequency losses. In contrast, electronic absorption dominates when metallic films are continuous. Such free electron absorption (often modeled by Drude absorption) is characterized by low frequency absorption. Free electron absorption is observed to dominate the low frequencies in the as-deposited films [Fig. 1(a)]. Upon annealing, however, high frequency scattering starts to dominate due to film roughening [Figs. 1(b) and 1(c)]. On the other hand, transmission of infrared light is not affected by the presence of TaN [Fig. 1(a)], which, together with the complete absence of the optical effect (i.e., no Si phonon modes as explained in Sec. III A 3) indicates that metallic properties of TaN are weak compared to those of Ru and Pt.

Considering slightly higher extinction coefficients of bulk Ru compared to those of Pt in the given infrared range,⁹ more absorption would be expected with Ru. But the lower transmittance, thus higher absorbance of HfO_2/Pt in Fig. 1(a) suggests either relatively thicker Pt layers or weakened free electron absorption due to higher degree of surface oxidation of Ru. Each metal layer has a distinct reactivity toward the ambient after exposure to air. Nonconductive oxide (i.e., different from RuO_2) is known to grow on Ru which is exposed to air at room temperature.¹⁰ Pt is not easily oxidized and oxidation is only limited to the surface to a lesser degree, causing it to have higher absorption. On the other hand, the transmission of HfO_2/TaN is almost the same as that of HfO_2 , suggesting that the deposited TaN film has low conductivity due to O-rich composition because ultrathin TaN is permeated with oxygen upon exposure to air.

Upon annealing, a dramatic change in the baseline is observed for Ru and Pt samples, with the latter having twice as much change in absorption amplitude than the former (see Figs. 1(b) and 1(c)). Reduction in surface Ru-oxides and Pt-oxides (i.e., $\text{MO}_x \rightarrow \text{M} + 0.5\text{xO}_2$, where $\text{M} = \text{Ru}$ or Pt) occurs at 400–500 °C,^{11–13} which causes the further increase in absorption observed in 400 °C annealed Ru and 400–500 °C annealed Pt samples. Higher absorption in the lower wave-numbers at these temperatures also confirms enhanced Drude absorption by increased number of free carriers after reduction.

The absorbance starts to decrease at 500 °C with Ru [Fig. 1(b)] and 600 °C with Pt [Fig. 1(c)]. This sudden decrease in absorption is related to an initiation of metal agglomeration. During annealing, thin metal films on dielectric surfaces can agglomerate into clusters to reduce the interface and metal surface energies.¹⁴ Metal agglomeration is accompanied by a drastic change in the dielectric constants because the initially continuous metal films are disconnected into islands, thus exposing the underlying dielectrics and changing the conductivity.^{15,16} The higher absorption with frequency (i.e., scattering) is also an indication of enhanced roughness due to agglomeration. In contrast, the baseline change and shift are negligible in HfO_2/TaN throughout the whole thermal process (not shown).

The baseline shift in HfO_2/Ru after 500 °C annealing [Fig. 1(b)] suggests that the change in optical properties is gradual, most likely limited to the top layers except for 950 °C annealing. The dramatic baseline shift observed in annealed HfO_2/Pt [Fig. 1(c)] suggests that there are more severe compositional changes through interdiffusion of elements.

2. Thermal evolution and compositional changes

More detailed thermal evolution of each film is shown in the differential infrared vibrational spectra in Fig. 2. In general, the HfO_2 and HfO_2/TaN film evolutions are similar except that amorphous HfO_2 films crystallize into the monoclinic phase at 500 °C without any metal capping (a) and at 600 °C with TaN (b). The characteristic monoclinic HfO_2 modes¹⁷ at 602, 650, 791 (798) cm^{-1} [HfO_2 longitudinal optical mode (LO)] and 513 cm^{-1} [transverse optical mode (TO)] are clearly observed in Figs. 2(a) and 2(b). The increase in crystallization temperature by 100 °C with the TaN capping layer can be due to the constraint of SiO_2 and TaN which increases the misfit strain energy upon crystallization.¹⁸

Accompanying HfO_2 crystallization, the underlying Si–O bonds are disrupted as evidenced by the negative SiO_2 phonon modes at 1050 (or 1054) and 1256 cm^{-1} . The estimated thickness of affected SiO_2 derived from the integrated area is only ~ 1 Å. 1050/1256 cm^{-1} can be assigned to the TO_3/LO_3 asymmetric stretching mode which is directly related to the Si–O–Si angle configuration in the amorphous network.¹⁹ The lower position of TO_3 at 1050 cm^{-1} compared to the normal 1075 cm^{-1} indicates that the averaged Si–O–Si angle is lower.²⁰ LO_3 is much less sensitive than that of the TO_3 mode to the variation in the Si–O–Si angle.²¹ The first interface layer of Si–O bonded to HfO_2 layer is

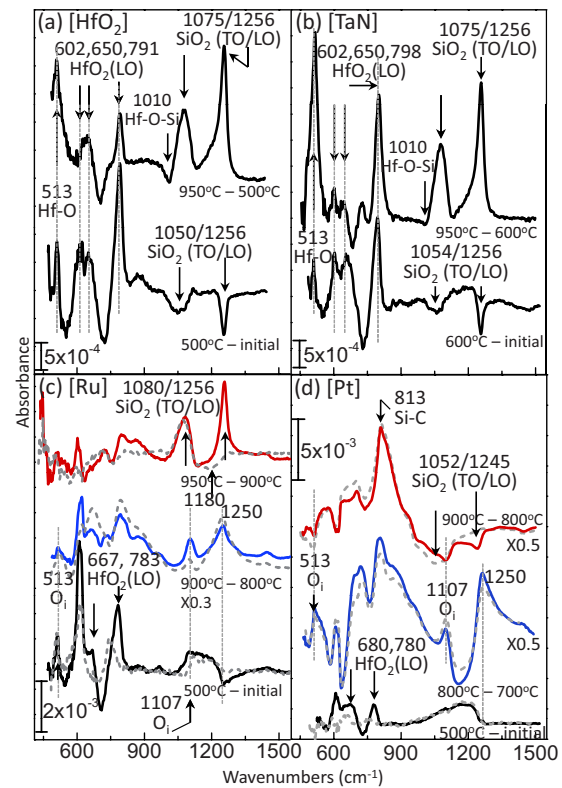


FIG. 2. (Color online) Differential infrared vibrational spectra of annealed (a) HfO_2 , (b) HfO_2/TaN , (c) HfO_2/Ru , and (d) HfO_2/Pt . The spectra references are specified in the figure as either the initial surface before annealing (initial) or the annealed surface at lower temperature where appropriate. Incidence angle close to the Brewster angle is used for all spectra except for gray dotted spectra in (c) and (d) which are measured with near-normal incidence. Baselines of spectra in (c) and (d) are corrected for clarification. Elements in square brackets indicate the top layer of each stack.

necessarily in the form of a suboxide silica network with the interfacial stress, which can lead to the lower bonding angle. It suggests that initial crystallization is accompanied by a slight disruption of the Si–O bonds in the near vicinity of HfO_2 .

The negative shoulder at 1010 cm^{-1} in Figs. 2(a) and 2(b) can be assigned to interfacial Si–O–Hf bonds,²² disturbed at 700–800 °C with a lesser degree for HfO_2/TaN according to differential spectra (not shown). It is related to the effect of the morphological change in HfO_2 on the interfacial Si–O–Hf bonding configurations because further crystallization is still observed up to 800 °C.

Once HfO_2 has crystallized, additional interfacial SiO_2 starts to grow at 700 °C both for HfO_2 and HfO_2/TaN films, reaching approximately ~ 8 Å at 950 °C [Figs. 2(a) and 2(b)]. It is suspected that newly-formed grain boundaries of crystalline HfO_2 provide channels for residual OH impurities in the chamber and/or in the films to diffuse into the Si/ SiO_2 interface. Purging the system of residual water by baking the chamber and the films for 24 h over 100 °C before the high temperature thermal cycling does not significantly affect the subsequent interfacial SiO_2 growth, suggesting that the main source of O is in the bulk of films. It is also possible that weakly bonded oxygen atoms in the stacks, through redistribution of bonds,²³ or interstitial oxygen in HfO_2 , if any, through diffusion into the SiO_2/Si interface,²⁴ can contribute

to the additional oxidation upon annealing. Except the O diffusion, there is no interdiffusion of Hf and Si observed between HfO_2 and SiO_2 even at 950 °C anneal.

The baseline-corrected spectra of the annealed Ru and Pt in Figs. 2(c) and 2(d) are very different from those of TaN. For both Ru and Pt, HfO_2 crystallization occurs at 500 °C, 100 °C lower than the crystallization temperature with a TaN capping layer. This is because the constraint exerted by the top layer upon crystallization is reduced due to agglomeration of metal which is not observed with TaN. Between 500–900 (800) °C with Ru (Pt), the differential spectra are dominated by optical effects, burying actual changes in the chemical bonding, if any, under the substrate phonon contribution arising from an optical effect described in the Sec. III A 3.

At 950 °C bulk phonon modes are not dominant any more in HfO_2/Ru [Fig. 2(c)]. Instead, there is a slight increase in the intensity of SiO_2 TO/LO at 1080/1256 cm^{-1} and loss of HfO_2 related modes below 700 cm^{-1} . The additional thickness of SiO_2 is about 5 Å at 950 °C. The mode at 1256 cm^{-1} can be distinguished from the optical artifact found in the rest of other spectra in Fig. 2(c) by checking the LO characteristics; i.e., absent in the normal-incidence spectrum. A detailed structure of the SiO_2 phonon mode at 950 °C shows that there is also a negative peak centered at 1180 cm^{-1} which can be assigned to the asymmetric stretching of Si–O bonds. Even though the net result is the growth of SiO_2 , decomposition of Hf–O and Si–O bonds suggests that there is a partial collapse of these two layers. The partial loss of these bonds corresponds to the localized Hf-silicidation and Ru-silicidation which will be discussed below.

A striking contrast for HfO_2/Pt is that the underlying SiO_2 decomposes rather than grows with high-temperature annealing. The presence of bulk Si phonons and O interstitial complicates the spectrum, but the loss of SiO_2 at 900 °C is evident, observed as the negative absorption at 1052/1245 cm^{-1} of TO/LO of SiO_2 in Fig. 2(d). The integrated area under the lost SiO_2 phonon modes corresponds to approximately 2 nm, suggesting almost all SiO_2 layer is decomposed at 900 °C. The exposed bare Si substrate is then vulnerable to carbon contaminants in the system. Considering that C chemically bonds to silicon at elevated temperature, the mode at 813 cm^{-1} can be assigned to Si–C stretching vibration.

3. Optical effects on IR absorbance spectra

The presence of metal films on semiconductor can greatly affect optical spectra due to electric field variation at the interface. As studies on deposition of thin metal films by using infrared absorption spectroscopy are attracting growing attention in recent years, there is a need to distinguish optical effects for correct data analysis, which has not been done so far. Indeed, previous works have erroneously assigned spectral changes to chemical modification of the system without recognizing that optical effects could produce such observations.^{25,26} This section focuses, therefore, on the identification of optical artifacts observed in our study and on providing an explanation of these observations.

The features below 1500 cm^{-1} in both HfO_2/Ru and HfO_2/Pt absorption spectra in Fig. 1(a) are attributed to the substrate Si phonon modes as shown in the inset of panel (a). These large absorption variations are observed even though the sample temperature is well controlled during measurements, thus minimizing any possible variation in Si phonon absorption. Calculations show that the large negative absorption of the Si phonon spectrum (involving optical and acoustic transverse/longitudinal combination modes) in the inset of Fig. 1(a) is a result of a weakening of the electromagnetic field in the underlying Si layers below the continuous metallic film due to the high index of refraction of the capping metal.

Another optical effect arises from distinct morphology changes in the metallic film upon annealing. Substantial agglomeration of initially continuous metal films gives rise to enhancement of the electric field at the upper interface. Thus, upon annealing from 500 to 900 (800) °C of Ru (Pt) samples [Figs. 2(c) and 2(d)] the differential spectra are now dominated by *positive* Si phonon modes and other bulk modes below 1500 cm^{-1} . For instance, the modes at 1107 cm^{-1} and 513 cm^{-1} in Figs. 2(c) and 2(d) correspond to the asymmetric stretching and bending of oxygen interstitial in the Si *bulk* (O_i), respectively. The bands at 610–630 cm^{-1} (TO+TA), 740 cm^{-1} (LO+LA), 818 cm^{-1} (TO+LA), 890 cm^{-1} (TO+LO), and 970 cm^{-1} (TO+TO) all arise from two phonon absorption of *bulk* Si.²⁷ All these modes are greatly enhanced compared to typical surface absorption. It is proposed that the strong positive absorption upon annealing is due to *surface-enhanced IR absorption* (SEIRA) promoted by the roughened metal surface.^{16,28} The electromagnetic enhancement, and thus the absorption of IR radiation can be generated with a metal underlayer and overlayer.²⁹ In addition, the presence of an inhomogeneous surface such as rough metal films can increase IR intensities through local field enhancement.^{30,31} Agglomeration with further annealing increases roughness of the initially smooth metal overlayer, which in turn affects the IR absorption. SEIRA is usually utilized to enhance absorption bands of adsorbed molecules on metal particles. In our case the enhancement is manifested as amplified phonon modes of the underlying Si substrate.

The feature near 1250 cm^{-1} is very close to LO of O–Si–O asymmetric stretching vibrations of SiO_2 but its presence in the normal-incidence spectra (gray) indicates that it does not have the LO characteristics (i.e., polarized perpendicular to the surface). Between 500 and 600 °C annealing, the mode at 1250 cm^{-1} initially has negative amplitude and turns to the positive with further annealing up to 900 (800) °C for Ru (Pt), which eventually cancels out the contribution from this region in the absorbance spectra referenced to the initial surface (not shown). The origin of this mode is not certain but it is most likely attributed to the optical artifacts described above rather than actual changes in the chemical bonding.

It should be emphasized, however, that agglomeration results from the use of ultrathin metal layers. For typical CMOS processing, the metal gate is thicker and buried (protected by other layers) so that agglomeration is not expected. Now that potential artifacts created by optical effects are

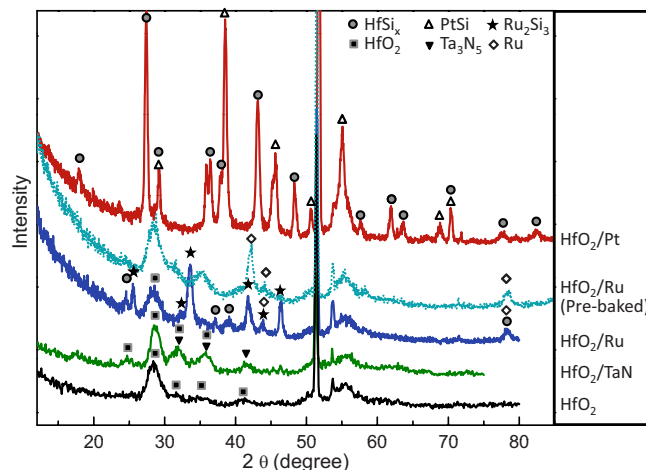


FIG. 3. (Color online) Glancing incidence (0.5°) XRD of HfO_2/Pt , HfO_2/Ru , $\text{HfO}_2/\text{Ta}_3\text{N}_5$ and HfO_2 stacks annealed for 20 s in N_2 up to 950°C . Note that silicidation is almost completely suppressed in HfO_2/Ru annealed after the system has been baked at $>100^\circ\text{C}$ over 24 h (pre-baked).

identified, changes in chemical bonds of the dielectric layers can be distinguished by investigating polarization-dependent IR absorption spectra as described above.

B. Silicide formation (XRD)

Figure 3 shows glancing incidence (0.5°) XRD of HfO_2/Pt , HfO_2/Ru , $\text{HfO}_2/\text{Ta}_3\text{N}_5$, and HfO_2 stacks measured after annealing at 950°C . All these stacks are amorphous before thermal processes. The most striking feature is that the silicide peaks (HfSi_x , PtSi) of annealed HfO_2/Pt are so prominent that there is no clear evidence of the monoclinic HfO_2 phase which is clearly observed for the other samples. In addition to hafnium silicide, top metal silicide formation is observed for both HfO_2/Ru and HfO_2/Pt . Figure 3 also shows that residual hydroxyl groups in the system are required to drive silicide formation in the HfO_2/Ru system. When annealing is carried out after the system has been baked at $>100^\circ\text{C}$ over 24 h, Hf-silicidation or Ru-silicidation is completely suppressed as shown in the dotted “ HfO_2/Ru (pre-baked)” spectrum in Fig. 3. In contrast, formation of HfSi_x and PtSi after annealing the HfO_2/Pt stack is not affected by preceding bakeout.

Unlike Ru or Pt, the presence of TaN as a gate electrode does not induce any silicidation. Only 2θ peaks corresponding to monoclinic HfO_2 and cubic (or tetragonal) TaN are observed [Fig. 3 “ HfO_2/Ru ”]. XRD data in Fig. 3 show that no silicide is formed in the bare HfO_2 films [Fig. 3 “ HfO_2 ”] with the current thickness of HfO_2 (4 nm) and SiO_2 (2 nm) upon 950°C annealing for 20 s. Capping with Ru or Pt has a catalytic effect on the silicide formation with Pt having much more enhanced effects. The high work function of Ru and Pt may make the decomposition of HfO_2 and SiO_2 more energetically favorable (with the presence of $-\text{OH}$ groups in the case of Ru). Once the interface between Ru/Pt and Si is established, silicidation is indeed known to occur readily.

C. Metal transport and silicide formation angle-resolved x-ray photoemission spectroscopy (ARXPS)

In the XPS spectra in Fig. 4, the binding energy of the bulk Si^0 $2p$ at 99.3 eV is used as the reference. When Si^0 $2p$ is not visible, C $1s$ peak of adventitious carbon (from exposure to air) is set at 285.0 eV as the binding energy reference. The deconvolution was carried out using a Lorentzian combined with a Gaussian and a least-squares fit procedure with a Shirley-type background subtraction (AANALYZER VER. 1.07 software).

Silicidation of Hf with Ru and Pt is also evidenced by the binding energy of the Hf $4f_{7/2}$ peak at 14.5 eV,^{1,32} which has a 0.5 eV narrower full width at half maximum than prior to annealing (deconvoluted in Figs. 4(a) and 4(d)). Si (or metal)-bound Ru $3d$ at 280.7 eV and Pt $4f$ and 72.9 eV are also evident in Figs. 4(b) and 4(e), respectively. The intensity of Si bound Hf is very low compared to that of O bound Hf in the annealed HfO_2/Ru [Fig. 4(a)], which is consistent with the low intensity of HfSi_x peaks of XRD data in Fig. 3. Hf-silicide and Pt-silicide are the dominant composition observed in XPS in the annealed HfO_2/Pt stack [Figs. 4(d) and 4(e)], also consistent with XRD.

The Hf^{4+} peak at 17.6 eV (17.3 eV) for $\text{HfO}_2/\text{Ru(Pt)}$ is close to that of the Hf-silicate,³³ suggesting Si infusion into the metal oxide to form a silicatelike compound. The position of the O $1s$ is 531.3 eV (532.7 eV) for $\text{HfO}_2/\text{Ru(Pt)}$ (not shown), which is close to that of oxygen in silicate, again consistent with the formation of a silicatelike phase.

The Si $2p$ core level is only visible after annealing of Ru and Pt samples due to agglomeration of metal and diffusion of Si. The contribution from SiO_2 at 103 eV is very small for the annealed HfO_2/Pt [Fig. 4(f)], consistent with *in situ* infrared absorption spectra in Fig. 2(d) showing the decomposition of SiO_2 . The large Si $2p$ contribution from 101.5 eV, unique to Pt samples [Fig. 4(f)] is close to Si–C binding energy, which is also consistent with IR spectra. The corresponding C $1s$ binding energy is expected in 283–284 eV.^{34–36} The lowest binding energy in C $1s$ core level spectra, however, is 284.4 eV (not shown), close to that of ubiquitous C contaminants. Even though C $1s$ at 284.4 eV is too high to be Si–C bonds, the stoichiometry of SiC derived from the corresponding area of Si $2p$ at 101.5 eV and C $1s$ at 284.4 eV is close to that of SiC; i.e., $\text{SiC}_{0.96}$, $\text{SiC}_{1.45}$, and $\text{SiC}_{1.24}$ at three different take-off angles (15° , 45° , and 75° respectively). In addition, the contribution of C $1s$ at 284.4 eV ($I_{\text{C } 1s \text{ at } 284.4}/I_{\text{all C } 1s}$) is larger toward the bulk, contradicting to what would be expected for ubiquitous C contaminants. Therefore, we cannot exclude the possibility that Si bound C, shifted by electrostatic effects, is an important part of the C $1s$ signal.

Contrary to the signal from the HfO_2/Pt and HfO_2/Ru systems, there is almost no change in the oxidation state of Hf of the annealed HfO_2/TaN film [Fig. 4(g)] except for a slight decrease in the peak width due to crystallization. XPS Hf $4f$ core level spectrum of annealed HfO_2 films without any metal layers is very similar to that of HfO_2/TaN in Fig. 4(g), both of which show no sign of silicidation. Deconvolution of the Ta $4f$ prior to annealing [Fig. 4(h)] shows that

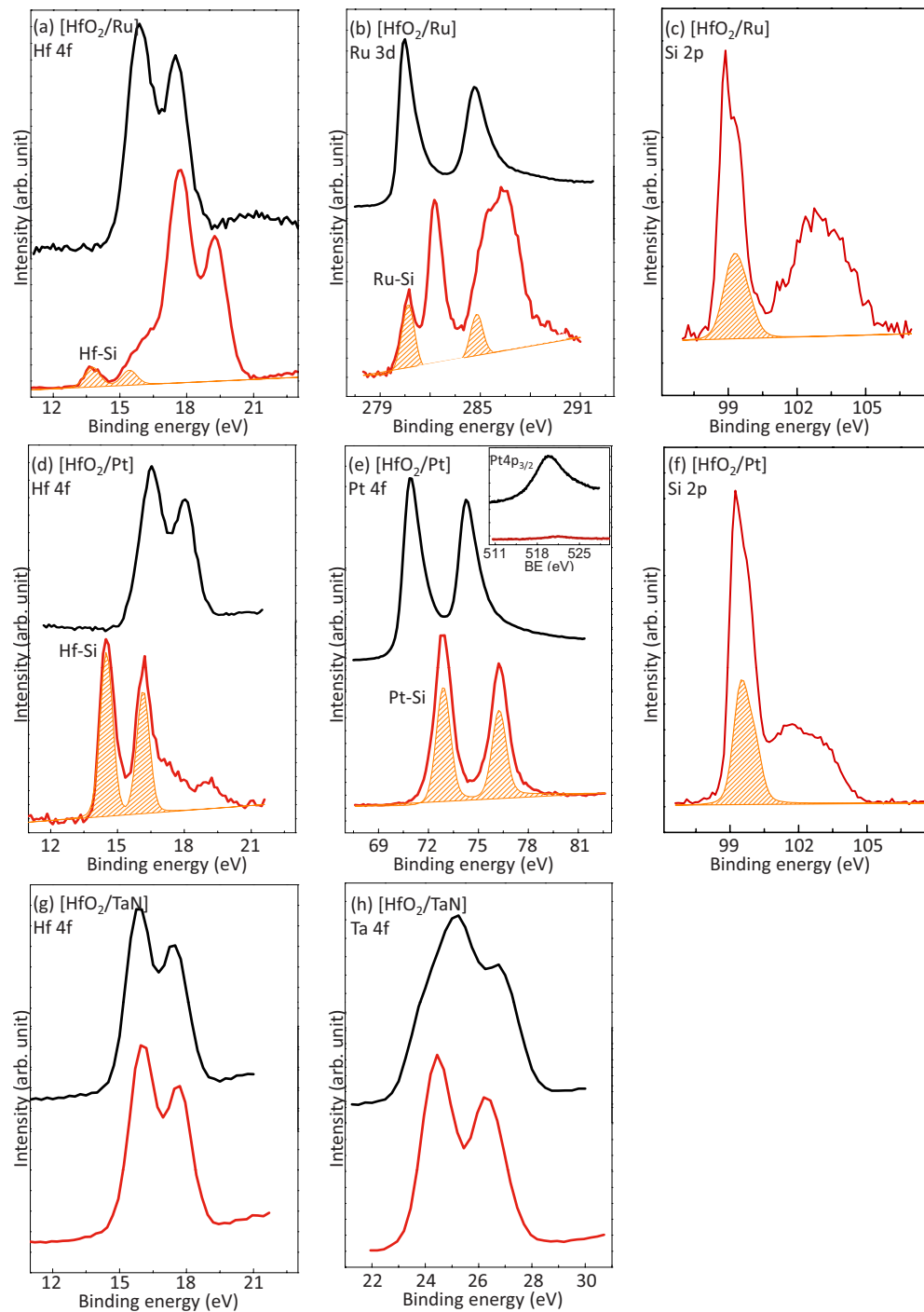


FIG. 4. (Color online) XPS spectra of core level of (a) Hf 4f, (b) Ru 3d, and (c) Si 2p of HfO₂/Ru, (d) Hf 4f, (e) Pt 4f, and (f) Si 2p of HfO₂/Pt, (g) Hf 4f and (h) Ta 4f of HfO₂/Ta₂N before (upper spectra in each panel) and after annealing (lower spectra in each panel). The inset of (e) is Pt 4p in a common scale for both spectra. The fits (patterned with oblique lines) are deconvoluted spectra of metals bonded to silicon. Si 2p is not visible before annealing with capping metal and even after annealing with TaN. Elements in square brackets indicate the top metal layer of each stack. The spin-orbit splitting is fixed at 1.7 eV for Hf 4f, 4.1 eV for Ru 3d, 3.3 eV for Pt 4f, 1.9 eV for Ta 4f, and 0.6 eV for Si 2p.

the initial film contains a mixture of N-bound and O-bound Ta, characterized by two components at 24.2 eV and 25.3 eV, respectively. After annealing HfO₂/Ta₂N, the binding energy of Ta 4f_{7/2} is shifted to 24.5 eV, characteristic of N-bound Ta and, therefore, suggesting a thermally-driven loss of oxygen. The absence of Si 2p even after annealing also suggests that Si diffusion is completely suppressed.

It is noteworthy that the intensity of Pt 4p is greatly diminished after annealing [inset of Fig. 4(e)]. Such a dra-

matic intensity decrease in the XPS upon annealing is not observed with other metal films (e.g., Ru and TaN). Loss of Pt atoms from the surface through diffusion seems to contribute to the diminished intensity of Pt core level spectra upon annealing.

The angle-resolved XPS with photoemission angles from 15° to 75° is used to analyze the depth distribution of each element of HfO₂/Ru and HfO₂/Pt after annealing (Fig. 5). The relatively high Si ratio in annealed HfO₂/Pt suggests

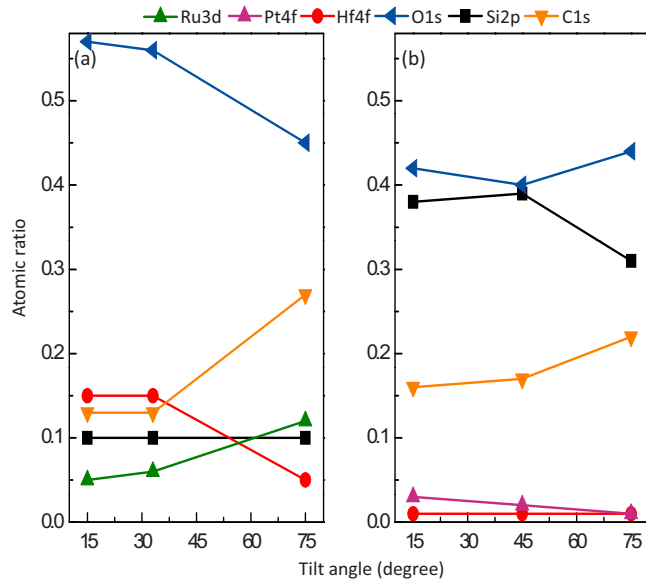


FIG. 5. (Color online) Atomic ratio according to ARXPS of the annealed (a) HfO₂/Ru and (b) HfO₂/Pt.

major loss of elements in the top layers and/or Si diffusion. Indeed the atomic ratio of Hf and Pt is very low throughout the stack compared to that of HfO₂/Ru. In addition, the Pt ratio is slightly increasing toward the bulk, suggesting metal diffusion toward the substrate. On the other hand, Ru shows the higher concentration toward the surface, expected when there is no Ru diffusion into the underlying layers.

D. Silicidation upon Si substrate exposure (AFM)

The rms roughness of all the investigated films before annealing is about 1–2 Å. After annealing, the roughness is slightly increased to 4 Å for both HfO₂ and HfO₂/TaN films (Figs. 6(a) and 6(b)). The annealed HfO₂/Ru is partially covered with round voids as shown in the microscopic image in the inset of Fig. 6(c). The rms is 3.4 nm outside of the void [left part of the Fig. 6(c)] and 10 nm inside the void [right part of the Fig. 6(c)]. The islands inside the void [right part of Fig. 6(c)] have depth on the same level as the Si substrate or even below the level [section analysis of Fig. 6(c)]. These observations suggest that these voids may be the

main location where silicidation takes place through metal diffusion. The annealed HfO₂/Pt surface is filled with craters under a microscopic view (not shown), probably as a result of desorption of volatile components. Its rms roughness is approximately 5 nm [Fig. 6(d)].

E. Silicide formation through decomposition of dielectrics and metal diffusion

The reaction between Ru (Pt) and HfO₂ to reduce HfO₂ is not favorable from a bulk thermodynamic point of view since a positive Gibbs free energy is expected for the Ru (Pt) and HfO₂ reaction of Ru(Pt) + HfO₂ → HfO_{2-x} + Ru(Pt)O_x.³⁷ Reduction in HfO₂ and SiO₂ with Ru and Pt is not necessarily through direct reaction between these materials. With Ru, residual OH impurities have been shown to be necessary to drive the Si/SiO₂/HfO₂/Ru system to form silicide (see Fig. 3). The catalytic effect of OH impurities in reducing HfO₂ has been reported previously with rhenium.⁸ It seems that external hydroxyl groups affect the stability of HfO₂ and SiO₂ during annealing. The partial loss of Hf–O and Si–O bonds at the 950 °C-annealed Ru sample observed in the IR spectra in Fig. 2(c) together with the AFM cross section in Fig. 6(c) indicates that the Si substrate is exposed at the center of islands after decomposition of dielectric layers. Elements can thus easily diffuse to form metal silicide (HfSi_x, RuSi_x) at these sites. It is well known that silicide is readily formed in the Ru/Si structure at elevated temperature through interdiffusion of species.^{38–40} The surface coverage by these islands is about 10%–20% under the microscopic view. The contribution of Si-bound Hf and Ru according to XPS in Figs. 4(a) and 4(b) is about 6% and 20%, respectively, close to the island coverage of the sample. The angle resolved XPS reveals that the Si (or Ru)-bound Ru 3*d* and Si-bound Hf 4*f* have higher fraction closer to the bulk, indicating silicide formation occurs near the Si substrate. On the other hand, the freed oxygen from decomposed HfO₂ and SiO₂ either desorbs as the volatile O₂, HfO_x, and SiO or diffuses into the lower interface as O to form SiO₂ outside the islands as evidenced by the net increase in SiO₂ LO/TO in Fig. 2(c).

In contrast to the localized silicidation observed with Ru, annealing with the presence of Pt strongly reduces both HfO₂

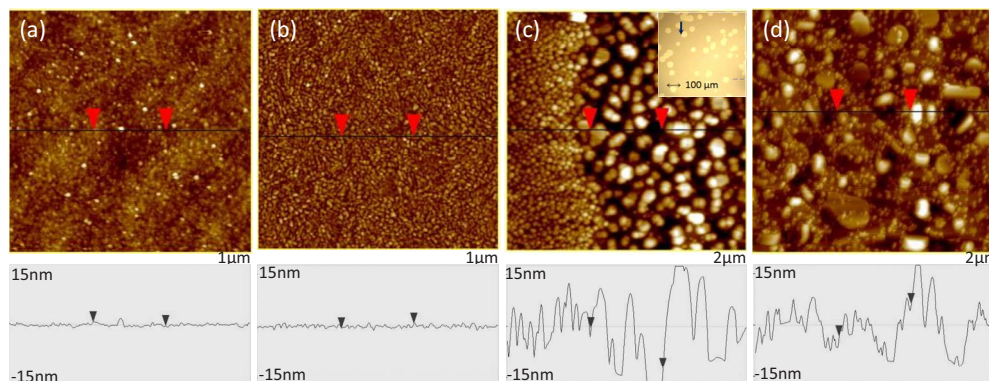


FIG. 6. (Color online) AFM surface images of (a) HfO₂, (b) HfO₂/Ta₂N₅, (c) HfO₂/Ru, and (d) HfO₂/Pt after annealed up to 950 °C in N₂ and section analyses (the lines denote the location of the sections). Note that 1 × 1 μm² for (a) and (b) and 2 × 2 μm² for (c) and (d) are probed. The inset of (c) shows the microscopic image of voids on the surface and the AFM is taken at the boundary indicated by an arrow.

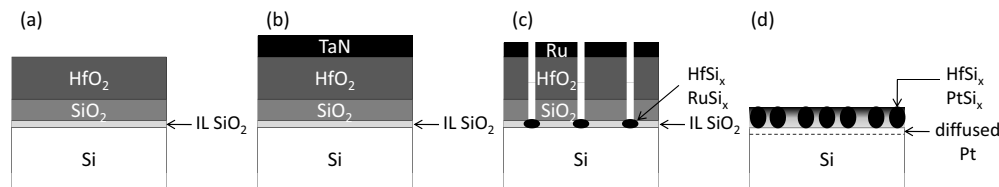


FIG. 7. Schematic view of structures of (a) $\text{SiO}_2/\text{HfO}_2$, (b) $\text{SiO}_2/\text{HfO}_2/\text{TaN}$, (c) $\text{SiO}_2/\text{HfO}_2/\text{Ru}$, and (d) $\text{SiO}_2/\text{HfO}_2/\text{Pt}$ after annealing up to 950 °C for 20 s in a N_2 ambient.

and SiO_2 of the whole stack regardless of the amount of hydroxyl impurities. The decomposition of SiO_2 at 900 °C is clearly shown in the infrared spectrum in Fig. 2(d). The apparent HfO_2 loss is buried under the higher-intensity of bulk phonons at the lower frequency range. But the absence of a clear m- HfO_2 phase in XRD of Pt samples (Fig. 3) and the weak intensity of O-bound Hf 4f [Fig. 4(c)] suggest that the film composition consisting of HfO_2 is very little.

The overall reduction in SiO_2 with Pt overlayer is quite contradictory to the oxygen vacancy (V_o) model for p-metal Fermi level pinning.⁴¹ According to this modified V_o model, oxygen is absorbed by Si substrate and electron is subsequently transferred to p-metal Fermi level upon annealing. But the IR vibrational spectra [Fig. 2(d)] show that SiO_2 decomposes at 900 °C and there is no evidence of a prior growth of the interfacial layer due to O adsorption at lower temperature. This observation suggests that the net loss of O through the formation of volatile components is greater than O diffusion into the Si/SiO₂ interface. Considering high diffusivity of Pt, it is possible that diffusion of Pt atoms into the underlying dielectrics upon annealing promotes the instability of the films, thus lowering the energy cost for decomposition of HfO_2 and SiO_2 . It is also possible that Pt acts as a catalyst to promote the decomposition [$\text{SiO}_2(\text{HfO}_2) + \text{Pt} \rightarrow \text{SiO}(\text{HfO})(\text{g}) + \text{O} + \text{Pt}$]. In other words, the charge exchange at the Pt/ HfO_2 interface creates a dipole field, which can weaken the Si–O and Hf–O bonds upon annealing. Pt is more electronegative than Hf. Thus the Pt–Hf interface bonds, if any, cause electron transfer to Pt. Generation of charged defects at the upper interface also creates built-in electric field. Indeed, deconvolution of Hf 4f and Pt 4f XPS spectra in Figs. 4(d) and 4(e) reveals the presence of spectral contributions at 15.3 eV and 71.5 eV, respectively, very close to the reported value at 15.1 eV and 71.6 eV for Hf–Pt bonds.⁴²

The diminished Pt atomic ratio after annealing [$\leq 3\%$, Fig. 5(b)] can be due to Pt diffusion into the Si substrate upon further annealing after Pt silicidation as well as due to agglomeration. It is known that Pt diffuses into Si through a dissociative, temperature-dependent mechanism ($\text{Pt}_i + V \leftrightarrow \text{Pt}_s$), and a kick-out mechanism ($\text{Pt}_i \leftrightarrow \text{Pt}_s + \text{Si}_i$),⁴³ where V stands for vacancy and subscripts i and s for interstitial and substitutional atoms, respectively. Ishiware *et al.*⁴⁴ have reported 53% platinum diffusion into Si for a 2 h 800 °C annealed PtSi sample by backscattering spectrometry. In our case, PtSi is formed on the Si surface after decomposition of SiO_2 and HfO_2 at 900 °C. Upon further annealing it is very likely that Pt diffuses into the Si bulk and dissolves interstitially and/or substitutionally in silicon.

Another reason for the very low atomic ratio of Pt after annealing [Fig. 5(b)] could be Pt loss through volatile PtO_x formation.^{45–47} The Gibbs free energy of platinum oxide formation is very high (e.g., >1000 kJ/mol at 500 °C for the reaction $2\text{Pt} + \text{HfO}_2 \rightarrow \text{Hf} + 2\text{PtO}$), which makes Pt oxidation very unfavorable. But if there is any oxidation of agglomerated platinum particles with high temperature annealing (≥ 900 °C), it is possible that the equilibrium is shifted further to the side of the platinum oxide formation as more platinum oxide evaporates due to its volatility.^{46,47}

In general, the oxidation of noble metals such as Ru and Pt is thermodynamically not favorable. But the fact that Ru and Pt deposition is carried out in an external system after HfO_2 film growth suggests that the interface between metal and HfO_2 is O rich. Moreover oxygen is known to diffuse through thin Ru and Pt films through grain boundaries upon exposure to air.⁴⁸ This O-rich interface might induce oxidation of interface metal during annealing because the highly electronegative oxygen atom can attract electrons from metal, thus forming Ru(Pt)–O bonds. Indeed the higher oxidation state of Ru at 282.3 eV [Fig. 4(b)] is very close to that of nonconducting Ru oxides.⁴⁹

A schematic of structures of each gate stacks after 950 °C annealing is presented in Fig. 7.

The presence of Ru and Pt is essential for the reduction in the underlying dielectric films because no such silicidation is observed in the annealed HfO_2 or HfO_2/TaN films. Ru and Pt can act like electron sinks. The electrons from the oxygen vacancy level (V_o) from HfO_2 can transfer into the Fermi level of these high-work function metals,⁵⁰ thus making the HfO_2 reduction energetically more favorable. It is noteworthy that silicidation of the annealed gate stack with a thicker 150 nm Ru metal layer is very much suppressed whereas that of 200 nm Pt is as strong as the thin 2 nm Pt gate stacks. This suggests that morphological changes (voids) observed on annealed 2 nm Ru samples play a role in enhancing metal silicidation. On the other hand, silicidation takes place with the presence of Pt irrespective of Pt film thickness, indicating that the process is intrinsic.

IV. CONCLUSIONS

The distinct effects of thin high-work function metals, TaN, Ru, and Pt, on the thermal stability of Hf-based gate stacks have been investigated using *in situ* FTIR and *ex situ* surface characterization techniques. The compositional and morphological changes in annealed $\text{SiO}_2/\text{HfO}_2$ are relatively moderate, showing HfO_2 crystallization followed by additional interfacial SiO_2 layer growth. With Ru and Pt, how-

ever, metal silicidation is observed through decomposition of SiO_2 and HfO_2 . With Ru, hydroxyl impurities are indispensable in silicidation which is constrained to void nucleation sites which cover only $\sim 10\%$ – 20% of surface area. The data suggest that metal silicidation takes place in areas where the Si substrate is exposed due to decomposition of dielectric layers. The higher degree of metal silicide formation is observed with Pt together with a major decomposition of HfO_2 and SiO_2 . Finally, the results of annealed TaN-gate stacks are very similar to those without any capping metal layer; i.e., crystallization of HfO_2 and interfacial SiO_2 growth without any detectable metal diffusion.

ACKNOWLEDGMENTS

This work was supported by the National Science Foundation (Grant No. CHE-0415652).

- ¹H. T. Johnson-Steigleman, A. V. Brinck, S. S. Parihar, and P. F. Lyman, *Phys. Rev. B* **69**, 235322 (2004).
- ²N. Miyata, T. Nabatame, T. Horikawa, M. Ichikawa, and A. Toriumi, *Appl. Phys. Lett.* **82**, 3880 (2003).
- ³Y. Wang, M. Dai, M. T. Ho, L. S. Wielunski, and Y. J. Chabal, *Appl. Phys. Lett.* **90**, 022906 (2007).
- ⁴C. Gaumer, E. Martinez, S. Lhostis, C. Wiemer, M. Perego, V. Loup, D. Lafond, and J. M. Fabbri, *J. Electrochem. Soc.* **156**, G78 (2009).
- ⁵Y. Sugimoto, M. Kajiwara, K. Yamamoto, Y. Suehiro, D. Wang, and H. Nakashima, *Thin Solid Films* **517**, 204 (2008).
- ⁶D. Machajdik, A. P. Kobzev, K. Husekova, M. Tapajna, K. Frohlich, and T. Schram, *Vacuum* **81**, 1379 (2007).
- ⁷F. Fillot, B. Chenevier, S. Maîtrejean, M. Audier, P. Chaudouët, B. Bochu, J. P. Sénateur, A. Pisch, T. Mourier, H. Monchoix, B. Guillaumot, and G. Passemard, *Microelectron. Eng.* **70**, 384 (2003).
- ⁸M. Copel, R. P. Pezzi, D. Neumayer, and P. Jamison, *Appl. Phys. Lett.* **88**, 072914 (2006).
- ⁹E. D. Palik, *Handbook of Optical Constants of Solids* (Academic, New York, 1998).
- ¹⁰S. Sharma and L. Hines, *IEEE Transactions on Components, Hybrids, and Manufacturing Technology* **6**, 89 (1983).
- ¹¹J.-H. Ahn, W.-Y. Choi, W.-J. Lee, and H.-G. Kim, *Jpn. J. Appl. Phys., Part 1* **37**, 284 (1998).
- ¹²M. Kadoshima, T. Aminaka, E. Kurosawa, T. Aoyama, Y. Nara, and Y. Ohji, *Jpn. J. Appl. Phys.* **47**, 2108 (2008).
- ¹³Y. Abe, M. Kawamura, and K. Sasaki, *Jpn. J. Appl. Phys., Part 1* **38**, 2092 (1999).
- ¹⁴W. W. Mullins, *Acta Metall.* **6**, 414 (1958).
- ¹⁵W. W. Mullins, *J. Appl. Phys.* **28**, 333 (1957).
- ¹⁶A. E. Bjerke, P. R. Griffiths, and W. Theiss, *Anal. Chem.* **71**, 1967 (1999).
- ¹⁷X. Zhao and D. Vanderbilt, *Phys. Rev. B* **65**, 233106 (2002).
- ¹⁸G. Pant, A. Gnade, M. J. Kim, R. M. Wallace, B. E. Gnade, M. A. Quevedo-Lopez, and P. D. Kirsch, *Appl. Phys. Lett.* **88**, 032901 (2006).
- ¹⁹C. T. Kirk, *Phys. Rev. B* **38**, 1255 (1988).
- ²⁰E. Fogarassy, C. Fuchs, A. Slaoui, S. de Unamuno, J. P. Stoquert, W. Marine, and B. Lang, *J. Appl. Phys.* **76**, 2612 (1994).
- ²¹R. A. B. Devine, *Appl. Phys. Lett.* **68**, 3108 (1996).
- ²²M. T. Ho, Y. Wang, R. T. Brewer, L. S. Wielunski, Y. J. Chabal, N. Moumen, and M. Boleslawski, *Appl. Phys. Lett.* **87**, 133103 (2005).
- ²³T.-C. Tien, L.-C. Lin, L.-S. Lee, C.-J. Hwang, S. Maikap, and Y. Shulga, *J. Mater. Sci.: Mater. Electron.*
- ²⁴G. He, Q. Fang, M. Liu, L. Q. Zhu, and L. D. Zhang, *J. Cryst. Growth* **268**, 155 (2004).
- ²⁵D. T. Hsu, F. G. Shi, S. Lopatin, Y. Shacham-Diamand, B. Zhao, M. Brongo, and P. K. Vasudev, *J. Mater. Sci. Lett.* **18**, 1465 (1999).
- ²⁶T. Nguyen, S. He, and L. J. Charnesky, in *Initial Stage of CVD Copper Deposition on TEOS Oxide*, MRS Symposia Proceedings Vol. 403 (Materials Research Society, Pittsburgh, PA, 1996).
- ²⁷F. A. Johnson, *Proc. Phys. Soc.* **73**, 265 (1959).
- ²⁸A. Hartstein, J. R. Kirtley, and J. C. Tsang, *Phys. Rev. Lett.* **45**, 201 (1980).
- ²⁹Y. Ishino and H. Ishida, *Appl. Spectrosc.* **42**, 1177 (1988).
- ³⁰F. Maroun, F. Ozanam, and J. N. Chazalviel, *J. Phys. Chem. B* **103**, 5280 (1999).
- ³¹H. Metiu, *Prog. Surf. Sci.* **17**, 153 (1984).
- ³²A. de Sierro, C. R. Fluchter, D. Weier, M. Schurmann, S. Dreiner, C. Westphal, M. F. Carazzolle, A. Pancotti, R. Landers, and G. G. Kleiman, *Phys. Rev. B* **74**, 075319 (2006).
- ³³H. Kato, T. Nango, T. Miyagawa, T. Katagiri, K. S. Seol, and Y. Ohki, *J. Appl. Phys.* **92**, 1106 (2002).
- ³⁴Y. Mizokawa, K. M. Geib, and C. W. Wilmsen, *J. Vac. Sci. Technol. A* **4**, 1696 (1986).
- ³⁵V. M. Bermudez, *J. Appl. Phys.* **63**, 4951 (1988).
- ³⁶S. Sayan, E. Garfunkel, T. Nishimura, W. H. Schulte, T. Gustafsson, and G. D. Wilk, *J. Appl. Phys.* **94**, 928 (2003).
- ³⁷I. Barin, O. Knacke, and O. Kubaschewski, *Thermochemical Properties of Inorganic Substances (Supplement)* (Springer-Verlag, Berlin, 1977).
- ³⁸E. V. Jelenkovic, K. Y. Tong, W. Y. Cheung, and S. P. Wong, *Semicond. Sci. Technol.* **18**, 454 (2003).
- ³⁹Y. Matsui, Y. Nakamura, Y. Shimamoto, and M. Hiratani, *Thin Solid Films* **437**, 51 (2003).
- ⁴⁰L. Ley, Y. Wang, V. N. Van, S. Fisson, D. Souche, G. Vuye, and J. Rivory, *Thin Solid Films* **270**, 561 (1995).
- ⁴¹Y. Akasaka, G. Nakamura, K. Shiraishi, N. Umezawa, K. Yamabe, O. Ogawa, M. Lee, T. Amiaka, T. Kasuya, H. Watanabe, T. Chikyow, F. Ootsuka, Y. Nara, and K. Nakamura, *The Japan Society of Applied Physics* **45**, L1289 (2006).
- ⁴²G. K. Wertheim, D. N. E. Buchanan, and J. H. Wernick, *Phys. Rev. B* **40**, 5319 (1989).
- ⁴³S. Mantovani, F. Nava, C. Nobili, and G. Ottaviani, *Phys. Rev. B* **33**, 5536 (1986).
- ⁴⁴H. Ishiwaru, K. Hikosaka, and S. Furukawa, *J. Appl. Phys.* **50**, 5302 (1979).
- ⁴⁵H. Jehn, *J. Less Common-Met.* **78**, 33 (1981).
- ⁴⁶M. Rubel and M. Pszonlcka, *J. Mater. Sci.* **21**, 241 (1986).
- ⁴⁷M. Rubel, M. Pszonicka, and W. Palczewska, *J. Mater. Sci.* **20**, 3639 (1985).
- ⁴⁸R. Schmiedl, V. Demuth, P. Lahnor, H. Godehardt, Y. Bodschnwinna, C. Harder, L. Hammer, H. P. Strunk, M. Schulz, and K. Heinz, *Appl. Phys. A: Mater. Sci. Process.* **62**, 223 (1996).
- ⁴⁹P. Froment, M. J. Genet, and M. Devillers, *J. Electron Spectrosc. Relat. Phenom.* **104**, 119 (1999).
- ⁵⁰K. Shiraishi, K. Yamada, K. Torii, Y. Akasaka, K. Nakajima, M. Konno, T. Chikyow, H. Kitajima, and T. Arikado, *The Japan Society of Applied Physics* **43**, L1413 (2004).